Merging bound states in the continuum in the geometrical parameter space

Shiwang Yu,[1] Zhancheng Li,[1,*] Ruoheng Chai,[1] Wenwei Liu,[1] Wenyuan Zhou,[1] Hua Cheng,[1,†] and Shuqi Chen[1,2,3,‡]

[1]*The Key Laboratory of Weak Light Nonlinear Photonics, Ministry of Education, School of Physics and TEDA Institute of Applied Physics, Nankai University, Tianjin 300071, China*

[2]*School of Materials Science and Engineering, Smart Sensing Interdisciplinary Science Center, Nankai University, Tianjin 300350, China*

[3]*The Collaborative Innovation Center of Extreme Optics, Shanxi University, Taiyuan, Shanxi 030006, China*

(Received 30 November 2023; revised 6 February 2024; accepted 20 February 2024; published 5 March 2024)

Optical resonators can support bound states in the continuum (BICs) with infinite quality (Q) factors by eliminating radiation losses. However, practical optical resonators only support quasi-BICs with finite Q factors due to the scattering losses caused by inevitable fabrication defects. Merging multiple BICs in momentum space can improve the Q factors of resonators over a broad wavevector range. The dependence of a resonator on high-precision nanofabrication can also be decreased by improving the robustness of the Q factors of quasi-BICs against asymmetric structural parameters, which is much easier to realize high Q factors. Here, we propose an efficient method to merge multiple BICs in the geometrical parameter space by engineering a folded mode induced by Brillouin zone folding. Along with the topological charge evolution process in momentum space, this approach significantly improves the robustness of the Q factor of resonators against perturbations caused by geometric symmetry breaking and wavevector. Compared with fundamental isolated BICs, the merged BICs are more immune to structural disorders. Our approach provides a path to achieve robust ultrahigh-Q resonances, which holds immense potential in enhancing quantum and nonlinear effects, as well as improving the performance of optical sensors and nanolasers.

DOI: 10.1103/PhysRevB.109.115109

I. INTRODUCTION

Optical resonators, which can confine light in ultralong radiative lifetime are desirable for many nanophotonic applications [1,2]. Over the last few decades, a variety of mechanisms have been utilized to enhance light confinement, including total internal reflections (TIRs) and bound states in the continuum (BICs) [3,4]. Different from the guided modes, which are bound states and perfect trapped to the resonators due to TIRs, BICs reside inside the continuum but counterintuitively appear infinite radiation lifetime. In real optical systems, a true BIC with infinite Q factor is unobservable in the far-field condition and behave zero-resonance linewidth on the scattered spectrum. By contrast, the quasi-BICs with ultrahigh- and finite Q factors are utilized to enhance light-matter couplings since they provide effective radiation channels to be coupled to free space. Benefit from significantly enhanced light confinement, optical quasi-BICs have shown tremendous advantages in many applications, which allows nanolasers with lower thresholds and better performance [5–10], nonlinear devices with higher conversion efficiencies [11,12], optical modulators to be faster and smaller [13,14], biosensors to be more sensitive and compact [15–17], and enhanced quantum optical effects [18,19]. These applications are almost universal in various optical systems, such as optical waveguides and fibers, dielectric photonic crystals, optomechanical crystal, and metasurfaces [20–23]. Among the different types of BICs, symmetry-protected BICs, which originate from the symmetry mismatch between the external excitation modes and eigenmode profiles of the concerned systems, exist widely in various periodic extended structures [3,21,23,24]. Symmetry-protected quasi-BICs can be easily constructed by finely tuning the wavevectors or asymmetric geometrical parameters of the concerned systems that involve the brokens of the in-plane inversion symmetry when the systems exhibit a reflection or rotational symmetry [3]. The Q factors of the fundamental symmetry-protected quasi-BICs obey the scaling law $Q \propto 1/\alpha^2$ or $Q \propto 1/k^2$, where α is the geometrical perturbation factor and k is the wavevector that show how strong the perturbation of the ideal structure is [24]. This fundamental inverse-square scaling law results in that the Q factors of quasi-BICs are very sensitive to distortions of symmetry breaking. Furthermore, in practical nanofabrication, the radiative loss caused by the inevitable fabrication defects further limit the Q factors that resonators can reach. As a result, above-mentioned limitations bring higher sample fabrication requirements to achieve ultrahigh-Q resonances in the experiment.

Recently, merging multiple BICs in momentum space provide an effective method to improve the robustness of BICs against fabrication defects by promoting the Q factors over a wide wavevector range [25–29]. These merging-BIC approaches are based on the mechanism of topological charge conservation since a BIC correspond to the vortex center of the polarization vector distribution of far-field radiation,

*Corresponding author: zcli@nankai.edu.cn
†Corresponding author: hcheng@nankai.edu.cn
‡Corresponding author: schen@nankai.edu.cn

which carry an integer topological charge [30]. The merged BICs show a pronounced improvement of robustness of Q factors with an improved scaling rule from $Q \propto 1/k^2$ to $Q \propto 1/k^6$ [25,26]. When merging multiple BICs with high-order topological charges, the scaling laws can be promoted to $Q \propto 1/k^8$ [27]. By further combing the merged BICs with photonic band-gap mirrors to simultaneously forbit transverse and vertical leakages, an optical cavity with ultrahigh Q factors and ultrasmall model volumes can be constructed [28]. The mechanism of merging BICs in momentum space advances the realization of extremely low-threshold nanolasers and ultrasensitive chemical sensing [6–9,31]. Meanwhile, recent advancements have demonstrated that the impact of structural perturbations on the Q factors of quasi-BICs can be mitigated through the utilization of customized out-of-plane architectures or by reducing the symmetry of certain resonators [32,33]. These two design strategies reduce the dependence of the high-Q optical resonators on highly precise nanofabrication technique to some extent. However, they are limited to improve the robustness of Q factors against asymmetric geometrical factors and will lead to the reduced resonance efficiency. Hence, it would be of great significance to promote the robustness of the Q factors of BICs with respect to wavevector (k) and geometrical asymmetric factors (α) simultaneously.

Here, we demonstrate that the merging of BICs in the geometrical parameter space can produce robust high Q-factor resonances over broad geometrical asymmetric factor (α) and wavevector (k) ranges. One-dimensional (1D) and two-dimensional (2D) photonic crystal slabs (PCSs) are utilized to validate our scheme. By inducing gap-perturbed periodic symmetry breaking ($\alpha \neq 0$), the guided mode at the X point below the light line can be folded to the Γ point above the light line to form symmetry-protected BICs. The multiple BICs at different α can gradually approach the artificial BIC state at $\alpha = 0$ by simply varying the thickness of the PCS, eventually forming a merged BIC. The merged BIC state facilitates an evolution of the scaling rules of the Q factors from $Q \propto 1/\alpha^2$ to $Q \propto 1/\alpha^6$, which significantly improves the robustness of the Q factors against periodic symmetry breaking. Interestingly, the realized merged BICs is accompanied by the merging of two BICs in momentum space. Supercell simulations with disorder further prove that the Q factor of the merged BIC shows stronger tolerance on both fabrication defects and the wavevector. Our scheme is efficient for the realization of ultrahigh-Q resonances and it is expected to be extended various periodic photonic systems to enhance light-matter couplings.

II. DESIGNS OF THE 1D PCS WITH SYMMETRY-PROTECTED BICs

The 1D PCS, as illustrated in Fig. 1(a), is designed to achieve and analyze the merging of BICs in the geometrical parameter space. It consists of high refractive index α-Si grating fingers ($n = 3.48$) surrounded by uniform background medium with low refractive index ($n = 1.46$). The designed 1D PCS is infinitely long in the y direction and the width of the grating fingers is fixed as $w = 190$ nm. The other structural parameters used in simulation are $p = 350$ nm, $g = 350$ nm,

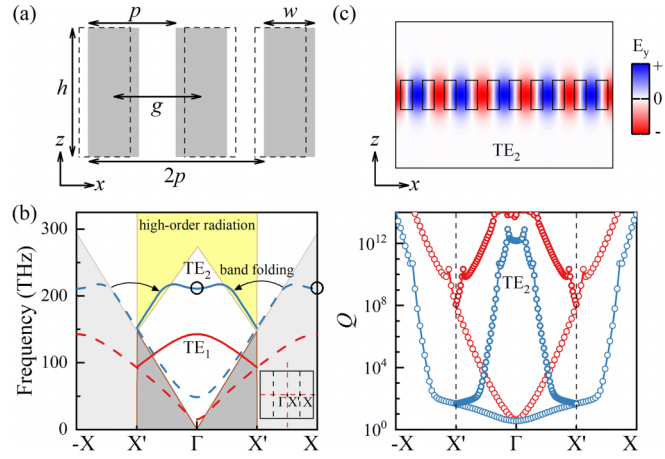

FIG. 1. Brillouin zone folding induced ultrahigh-Q guided resonances. (a) Schematic of the designed 1D PCS. (b) The left panel shows the simulated TE band dispersion diagrams of the original and perturbed slabs, which are plotted with dotted and solid lines respectively. Their Q factors are shown in the right panel, marked with hollow circles with thinner and thicker edge thickness respectively. The inset in the left panel shows the original and folded first Brillouin zone. The black arrows represent the band folding process. The shaded gray, white, and yellow areas represent the domain below the light line, zero-order, and higher-order radiation domains, respectively. (c) Calculated modal electric field profile E_y of the 1D PCS for the folded band TE_2, as marked with black circle at the Γ point in (b).

and $h = 544$ nm. All the simulation results are acquired by using finite element method. A more detailed description of numerical simulations is provided in Appendix.

When the gap size g between two adjacent grating fingers is equal to the period p of the original unit cell, the 1D PCS corresponds to an unperturbed 1D high-contrast grating. By displacing the grating fingers ($g \neq p$), the gap sizes between adjacent grating fingers are unequal, resulting in the periodic symmetry breaking. The gap perturbation produces a period-doubling $2p$ in the x direction. As a result, those modes previously at the edge of the first Brillouin zone (X point) now appear at the Γ point, which known as Brillouin zone folding [34–37]. The Brillouin zone folding causes the guided modes at the X point ($k_x = \pi/p$) below the light line to be shifted to the Γ point ($k_x = 0$) above the light line, enabling modes coupled to the far field. The simulated transverse electric (TE) band diagram and the corresponding calculated Q factors of the original and perturbed 1D PCS are shown in Fig. 1(b). Here, we focus on the TE_2 band shown as blue lines. The calculated Q factors of the folded TE_2 band showcase that a symmetry-protected BIC is formed at the Γ point, enabling ultrahigh Q factors over a broad wavevector range. The sharp drop in Q factors for larger wavevectors ($|k_x| \geqslant 0.11\pi/p$) is due to the fact that the modes are located in the higher-order radiation domain. The simulated modal profile of the TE_2 mode at the Γ point in multiple periods is shown in Fig. 1(c). The electric field distribution with antiphase and the same amplitude over every two adjacent gaps represents a nonradiative mode, in which the destructive interference in the far-field region results in the strong suppression of radiation losses.

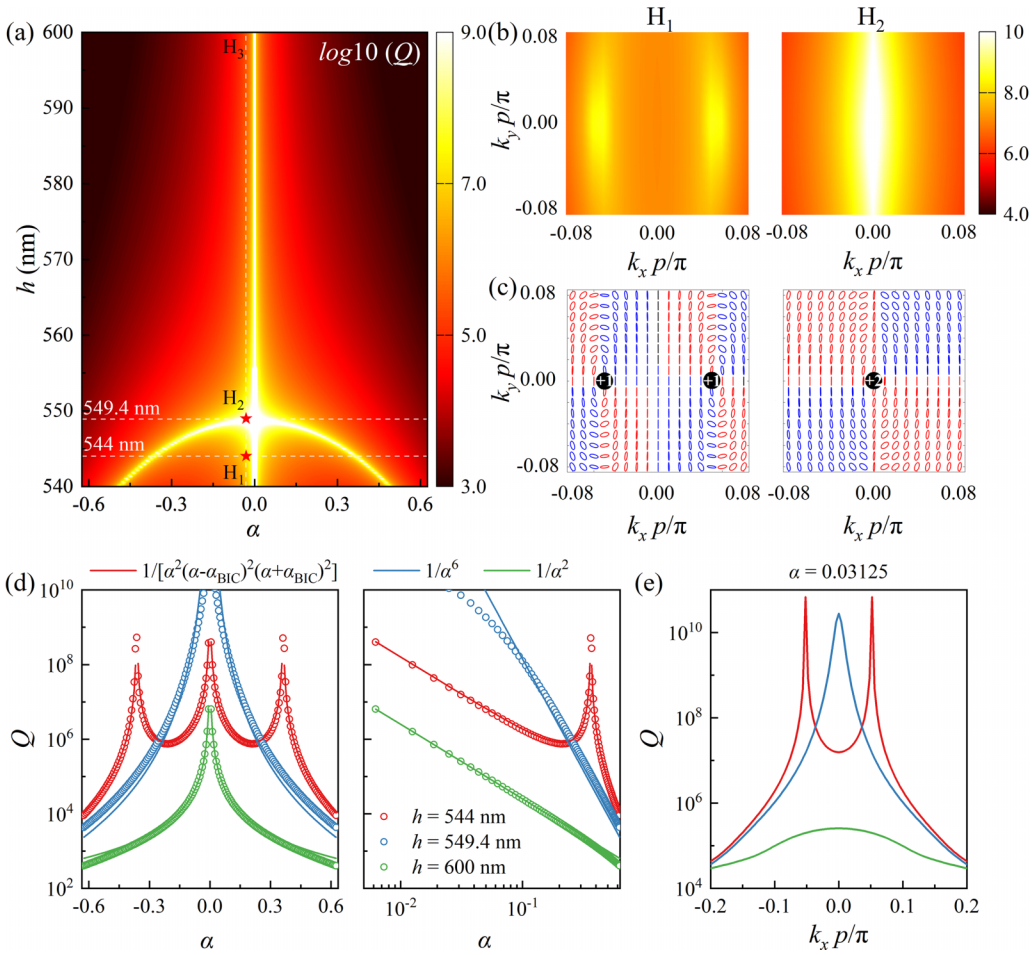

FIG. 2. Merging BICs in the geometrical parameter space based on the folded TE_2 mode. (a) The Q-factor evolution of the realized BICs with the variation of the perturbation factor α and the thickness of 1D PCS. Calculated (b) Q factors and (c) far-field polarization state distributions in momentum space at $h = 544$ nm (H_1) and 549.4 nm (H_2) for $\alpha = 0.03125$. The red (blue) ellipse denotes the left (right)-handed elliptic polarizations with different major axis orientations. (d) Simulated Q factors (scatter diagrams) and the corresponding fitting curves (solid lines) as a function of the perturbation factor α when the slab thickness $h = 544$ nm (H_1, red), $h = 549.4$ nm (H_2, blue), and $h = 600$ nm (H_3, green). (e) The evolution of Q factors with the variation of the wavevector k_x at different thicknesses for $\alpha = 0.03125$.

III. MERGING OF BICs IN THE GEOMETRICAL PARAMETER SPACE

The merging of BICs can be observed in the geometrical parameter space consisting of asymmetric factor α and the thickness h of the 1D PCS, as shown in Fig. 2(a). The asymmetric factor α is defined as $\alpha = (g - p)/(p - w)$, which represents the change of the transverse displacement of the grating finger relative to the original gap size. It should be noted that when $\alpha = 0$ ($g = p$), the BIC states actually stem from the guided mode, which can be dubbed artificial BICs [36–38]. The artificial BICs always exist for $\alpha = 0$. Meanwhile, two accidental BICs occur when $\alpha \neq 0$ and the thickness h is relatively small. The asymmetric factors α associated with the two accidental BICs exhibit equal absolute values and correspond to the same structural pattern, which are ensured by the presence of structural translational symmetry. With the increase of the thickness h, two accidental BICs gradually approach the artificial BIC at $\alpha = 0$. Ultimately, a merged BIC state occurs at $h = 549.4$ nm and exhibits ultrahigh Q factors over a broad asymmetry geometrical parameter range, which shows a similar evolution trend with the typical merging multiple BICs in momentum space [25–27].

We further analyze the Q-factor distributions in momentum space nearby the $\alpha = 0$ ($\alpha = 0.0325$) at the premerging (H_1, $h = 544$ nm) and merging (H_2, $h = 549.4$ nm) quasi-BIC states. As shown in Fig. 2(b), the merged quasi-BIC maintain higher Q-factor distributions nearby the Γ point over a broader momentum space range; the Q-factor distribution of premerging quasi-BIC state showcases two ultrahigh-Q accidental quasi-BICs in the positive and negative k_x direction and lower Q factors at the Γ point. These results indicate that the merging of BICs in the geometrical parameter space is accompanied by the merging of two BICs in momentum space. To reveal the topological nature of these BICs, we further analyze the polarization state distributions of far-field radiation in momentum space. A BIC is a singular point that corresponds to the vortex center of the polarization distribution of far-field radiation and carries an integer topological charge [30]. The topological charge is defined $q = \frac{1}{2\pi}\oint_C d\boldsymbol{k} \cdot \nabla_{\boldsymbol{k}}\phi(\boldsymbol{k})$, where C is a closed loop in momentum space surrounding the vortex center in a counterclockwise direction. Here,

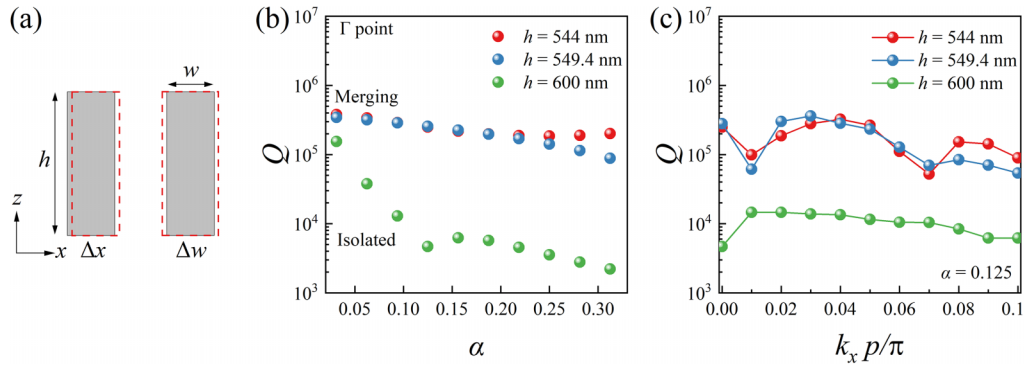

FIG. 3. Robustness of the merged BICs against fabrication disorder in both the geometrical parameter and momentum spaces for the 1D PCS. (a) Diagram of the unit cell of the designed structure, where the grey represents the ideal α-Si grating fingers and the dashed red boxes represents the disordered PCS. (b) The Q-factor evolution of the designed BICs with the variation of the asymmetric factor α at different thicknesses by applying disorder ($k_x = 0$). (c) The Q-factor evolution of the designed BICs with the variation of the k_x at different thicknesses by applying disorder ($\alpha = 0.125$). All the simulations were performed in a $15 \times 2p$ supercell arranged along the x direction and extend infinitely in the y direction.

$\phi(\boldsymbol{k}) = \frac{1}{2}\arg[S_1(\boldsymbol{k}) + iS_2(\boldsymbol{k})]$ is the angle of polarization vector at wavevector k and S_i is the Stokes parameter of the far field polarization vector [30,39]. As shown in Fig. 2(c), the calculated far-field polarization distributions at H_1 and H_2 showcase that polarization vortex centers are formed at the BIC point. When $h = 544$ nm (left panel, H_1), two off-Γ BICs occurs at the k_x axis, which carry the same $+1$ topological charge. When the height is increased to $h = 549.4$ nm (right panel, H_2), the two BICs merge at the Γ point and form a symmetry-protected BIC with a $+2$ topological charge. But this at-Γ symmetry-protected BIC is not stable and a further increase in height h causes the $+2$ topological charge BIC at the Γ point to split into two off-Γ BICs with $+1$ topological charge at the k_y axis [30,40]. Hence, it is the topological charge evolution process determined by the charge conservation that makes the Q factors of the merged BICs more robust in momentum space.

The distributions of Q factors with respect to the asymmetric factor α at three different grating finger heights are extracted from Fig. 2(a) to characterize the scaling properties of the Q factors of the BICs in the geometrical parameter space, as shown in Fig. 2(d). When the accidental BICs and symmetry-protected BIC coexist at $h = 544$ nm, which can be dubbed as pre-merging BIC state, the Q factor vary roughly as $Q \propto 1/[\alpha^2(\alpha - \alpha_{\mathrm{BIC}})^2(\alpha + \alpha_{\mathrm{BIC}})^2]$. As the height increases to $h = 549.4$ nm, the Q factors of the merged BIC decay as $Q \propto 1/\alpha^6$. With a further increase in height h, the Q factor of the after-merging isolated BIC ($h = 600$ nm) follows the scaling rule $Q \propto 1/\alpha^2$. Compared to the premerging and isolated BIC approximately follow the fundamental inverse-square scaling law in the vicinity of $\alpha = 0$, the Q factor of the merged BIC are orders of magnitude higher than these two scenarios. It is worth noting that the isolated BIC mentioned here is actually an ultrahigh-Q guided mode, not a real isolated BIC. Since it is located in the center of two off-Γ BICs in the k_y direction, it has a finite ultrahigh Q factor that follows the same scaling rules as the typical isolated BICs [24,25,30,40]. Figure 2(e) shows the Q factor distributions in the k_x direction at corresponding three different thicknesses h when $\alpha = 0.03125$ ($g = 355$ nm). The evolution of Q factors at three different thicknesses show similar trend as those with respect to α, which prove that our proposed merging-BIC design can significantly improve the robustness of the Q factor against the perturbations from geometrical symmetry breaking and wavevector.

In practical nanofabrication, the Q factors of BICs of fabricated samples always have large deviations from the ideal designed ones due to the structural disorder introduced by the inevitable fabrication defects. The structural disorder can introduce coupling between radiation modes at adjacent k points, thereby reducing the Q factors of practically realizable quasi-BICs. To validate the robustness of the merging-BIC design on fabrication errors, a 1D PCS composed of $15 \times 2p$ supercell with structural disorder in the x direction and extend infinitely in the y direction is studied. Two types of structural perturbations are considered in this paper, which are the fluctuations of the center positions (Δx) and widths (Δw) of the grating fingers, as shown in Fig. 3(a). According to the typical fabrication process precision, the errors Δx and Δw are set to fluctuate randomly from the ideal design with 1 nm standard deviation [41,42]. Figure 3(b) shows the calculated Q factors of the premerging, merging, and isolated quasi-BICs with the variation of asymmetric factor α. The Q factor of the merged quasi-BIC showcase a significant improvement of more than one order of magnitude for the large α compared to the standard isolated-BIC design, which is attributed to the improved scaling laws of Q factors with respect to α. The premerged BIC also shows robust ultrahigh-Q resonances due to the broad merging ranges when considering structural disorder or finite-size effect [6,25]. A similar enhancement effect of Q factor also occurs in momentum space, as validated by Fig. 3(c). These results prove that our merging-BIC design can considerably promote the robustness of the Q factor in both the geometrical parameter and momentum dimensions. The dips in Q-factor distribution at larger α and k points are caused by the coupling with other low-Q modes [35]. Taking the dip at $h = 600$ nm and $\alpha = 0.125$ as an example [Fig. 3(b), green line], the folded modes nearby the TE_2 mode at the Γ point occur due to the supercell with periodic boundaries, and the

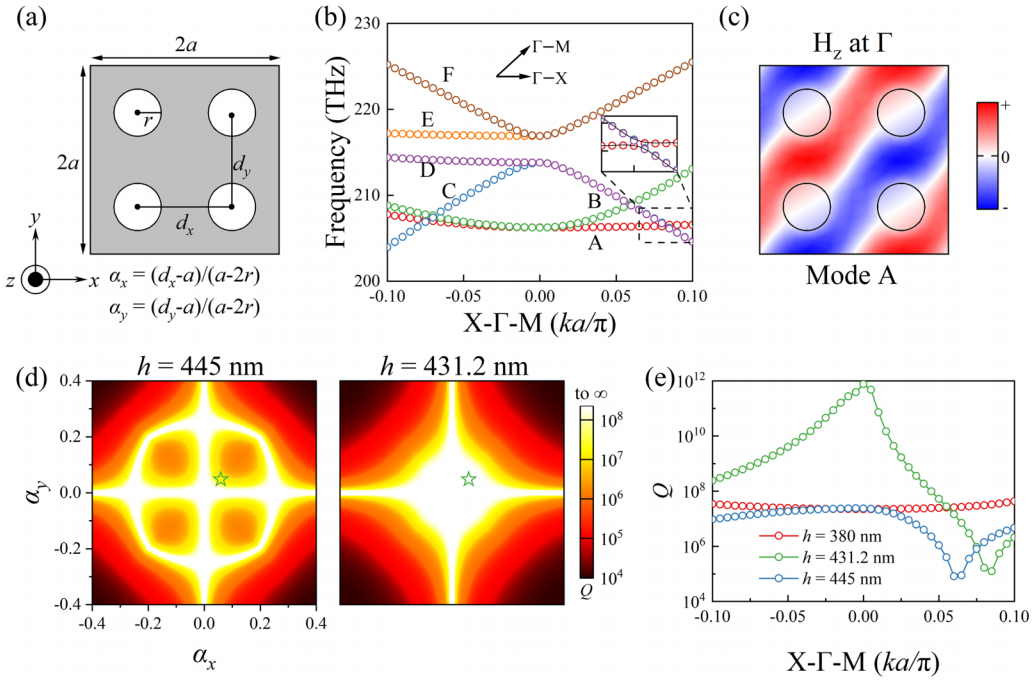

FIG. 4. Merging multiple BICs in the geometrical parameter space based on a 2D PCS. (a) Schematic of the unit cell of the designed 2D PCS. (b) Simulated TE-like band diagram of the perturbed PCS at $h = 431.2$ nm. The inset shows a magnification of the resonance avoided crossing behavior due to mode coupling. (c) The calculated field profile H_z of the mode A at the Γ point. (d) Calculated Q-factor distributions in the (α_x, α_y) geometrical parameter space at $h = 445$ nm (left) and $h = 431.2$ nm (right) at the Γ point. (e) The Q-factor evolution of mode A in momentum space at $h = 380$ nm, $h = 431.2$ nm and $h = 445$ nm, where $\alpha_x = \alpha_y = 0.05$ marked with the green pentagrams in panel (d).

couplings between the modes lead to the dip in the Q-factor distribution.

Although our design scheme is initially proposed in a 1D PCS system, the effect of merging multiple BICs in the geometrical parameter space can be generalized to other artificial nanostructures, such as 2D PCS and asymmetric metasurfaces [34,43]. We designed a 2D PCS as an example to prove the universality of our proposed scheme. As illustrated in Fig. 4(a), the designed PCS consists of α-Si slab with etched circular holes whose refractive index ($n = 1.46$) is the same as the uniform background. The structural parameters used in simulation are $a = 400$ nm and $r = 100$ nm. The gap distances between adjacent holes in the x and y directions are defined as d_x and d_y. The period of the PCS is $2a$ when the d_x and d_y are not equal to the original structural period a. As a result, the guide mode is folded into the continuum above the light line. Similar to the asymmetry factor α of the 1D perturbed PCS, we define $\alpha_x = (d_x - a)/(a - 2r)$ and $\alpha_y = (d_y - a)/(a - 2r)$ to represent the symmetry breaking of the 2D PCS. Figure 4(b) show the simulated TE-like band diagram of the perturbed PCS at $h = 431.2$ nm. Here, we focus on the mode A shown as red-dashed lines that is degenerated with mode B at the Γ point. The calculated magnetic field H_z of the mode A at the Γ point, as shown in Fig. 4(c), exhibits even symmetry and behaves as symmetry-protected BICs due to its incompatible symmetry with the radiating state, whose electromagnetic field vector is odd under C_2 operation [3,44,45]. To illustrate the merging of BICs in the geometrical parameter space in the 2D PCS, we further calculated the Q-factor distribution of the mode A with the variation of the asymmetry factor α_x and α_y at the Γ point when $h = 445$ nm and $h = 431.2$ nm. As shown in Fig. 4(d), the Q-factor distribution form a ring in the (α_x, α_y) geometrical parameter space at $h = 445$ nm. By decreasing the slab thickness, the high-Q ring can shrink and merge nearby the $\alpha_x = \alpha_y = 0$ point at $h = 431.2$ nm, thus significantly improving the robustness of the Q factor against geometrical asymmetric factor. We further calculated the Q-factor distributions of the quasi-BICs in momentum space when $\alpha_x = \alpha_y = 0.05$ under three different slab thicknesses, as shown in Fig. 4(e). The merged quasi-BIC ($h = 431.2$ nm) present ultrahigh Q factors over a large wavevector range nearby the Γ point and showcase an increase of more than two orders of magnitude compared to the premerging ($h = 445$ nm) and postmerging isolated quasi-BICs ($h = 380$ nm). Notice that the Q factor dips at larger wavevectors are due to the mode coupling between mode A and mode D [the inset in Fig. 4(b) shows the typical resonance avoided crossing behavior], which can be further eliminated by carefully optimizing the structural parameters of the slab. In line with the designed 1D PCS, the merging-BIC in the designed 2D PCS enhances the robustness of the Q factor in both the geometrical parameter and momentum spaces.

IV. CONCLUSIONS

In conclusion, different from the merging of BICs in momentum space, we have demonstrated merged BICs in the geometrical parameter space, resulting in robust ultrahigh-Q resonances over broad asymmetric geometrical parameter and wavevector ranges simultaneously. 1D and 2D PCSs have been designed to verify the proposed scheme. The guided modes in slabs were folded into the continuum to form

symmetry-protected BICs by merely varying the gap size of the two adjacent unit cells; multiple BICs in the geometrical parameter space were merged by adjusting the thickness of the slabs. The calculated far-field polarization distribution shows that the merging of BICs in the geometrical parameter space is accompanied by the topological charge evolution process in momentum space. Hence, the robustness of the merged BICs against practical nanofabrication defects has been significantly enhanced as verified by structural disorder simulations. Our approach provides a good candidate for the realization of ultrahigh-Q resonances, which can be further expanded to improve the performance of nanolasers and biosensors.

ACKNOWLEDGMENTS

This work was supported by the National Key Research and Development Program of China (Grants No. 2021YFA1400601, and No. 2022YFA1404501), the National Natural Science Fund for Distinguished Young Scholars (Grant No. 11925403), the National Natural Science Foundation of China (Grants No. 12122406, No. 12192253, No. 12274237, No. 12274239, and No. U22A20258), and the Natural Science Foundation of Tianjin (Grants No. 22JCYBJC01350, No. 22JCZDJC00400, and No. 22JCYBJC00800).

APPENDIX: NUMERICAL SIMULATION DETAILS

All the numerical simulation results were conducted using the commercial software COMSOL Multiphysics. The band structures and Q factors were calculated based on the eigenfrequency solver. The simulation of 1D PCS was conducted by employing a 2D model. In the calculated model, periodic (Floquet) boundary conditions were applied in the x direction of the unit cell and perfectly matched layers were set in the z direction. The maximum element sizes of the mesh in Si and background were set as 27.8 nm and 53 nm, respectively. In the analysis of robustness of the merged BICs against fabrication disorder, the simulations were conducted with a $15 \times 2p$ supercell, and the obtained results represent averaged values from five repeated simulations with different random perturbations. The considered perturbations Δx and Δw are set to fluctuate randomly from the ideal design with 1 nm standard deviation. In the specific simulation, random functions with normal distributions were set and different random seeds were used to generate random perturbations for each simulation. The simulation of the 2D PCS was implemented by employing a 3D model with periodic (Floquet) boundary conditions in the x and y directions and perfectly matched layers in the z direction. When solve the resonators with ultrahigh Q factors, the calculated Q factors are very sensitive to the mesh size and computational accuracy. When the ultrahigh Q factors are insensitive to asymmetric parameters, the variation of the mesh will lead to random fluctuations in Q factors while maintaining their elevated values [46]. Thus, the final Q factors in Fig. 4(d) are determined by averaging the values from four simulations to reduce the random oscillation in the Q-factor distribution. In each simulation, a mesh size smaller than one-twentieth of the wavelength was implemented within the structured region to improve simulation accuracy.

[1] Y. Akahane, T. Asano, B.-S. Song, and S. Noda, High-Q photonic nanocavity in a two-dimensional photonic crystal, Nature (London) **425**, 944 (2003).
[2] K. J. Vahala, Optical microcavities, Nature (London) **424**, 839 (2003).
[3] C. W. Hsu, B. Zhen, A. D. Stone, J. D. Joannopoulos, and M. Soljačić, Bound states in the continuum, Nat. Rev. Mater. **1**, 16048 (2016).
[4] P. Hu, C. Xie, Q. Song, A. Chen, H. Xiang, D. Han, and J. Zi, Bound states in the continuum based on the total internal reflection of Bloch waves, Natl. Sci. Rev. **10**, nwac043 (2023).
[5] A. Kodigala, T. Lepetit, Q. Gu, B. Bahari, Y. Fainman, and B. Kanté, Lasing action from photonic bound states in continuum, Nature (London) **541**, 196 (2017).
[6] M.-S. Hwang, H.-C. Lee, K.-H. Kim, K.-Y. Jeong, S.-H. Kwon, K. Koshelev, Y. Kivshar, and H.-G. Park, Ultralow-threshold laser using super-bound states in the continuum, Nat. Commun. **12**, 4135 (2021).
[7] Y. Ren, P. Li, Z. Liu, Z. Chen, Y.-L. Chen, C. Peng, and J. Liu, Low-threshold nanolasers based on miniaturized bound states in the continuum, Sci. Adv. **8**, eade8817 (2022).
[8] H. Zhong, Y. Yu, Z. Zheng, Z. Ding, X. Zhao, J. Yang, Y. Wei, Y. Chen, and S. Yu, Ultra-low threshold continuous-wave quantum dot mini-BIC lasers, Light: Sci. Appl. **12**, 100 (2023).
[9] S. Han, J. Cui, Y. Chua, Y. Zeng, L. Hu, M. Dai, F. Wang, F. Sun, S. Zhu, L. Li *et al.*, Electrically-pumped compact topological bulk lasers driven by band-inverted bound states in the continuum, Light: Sci. Appl. **12**, 145 (2023).
[10] X. Zhang, Y. Liu, J. Han, Y. Kivshar, and Q. Song, Chiral emission from resonant metasurfaces, Science **377**, 1215 (2022).
[11] Z. Liu, Y. Xu, Y. Lin, J. Xiang, T. Feng, Q. Cao, J. Li, S. Lan, and J. Liu, High-Q quasibound states in the continuum for nonlinear metasurfaces, Phys. Rev. Lett. **123**, 253901 (2019).
[12] K. Koshelev, S. Kruk, E. Melik-Gaykazyan, J.-H. Choi, A. Bogdanov, H.-G. Park, and Y. Kivshar, Subwavelength dielectric resonators for nonlinear nanophotonics, Science **367**, 288 (2020).
[13] I.-C. Benea-Chelmus, S. Mason, M. L. Meretska, D. L. Elder, D. Kazakov, A. Shams-Ansari, L. R. Dalton, and F. Capasso, Gigahertz free-space electro-optic modulators based on Mie resonances, Nat. Commun. **13**, 3170 (2022).
[14] X. Sun, J. Sun, Z. Wang, L. Wang, F. Qiu, and L. Wen, Manipulating dual bound states in the continuum for efficient spatial light modulator, Nano Lett. **22**, 9982 (2022).
[15] Y. Jahani, E. R. Arvelo, F. Yesilkoy, K. Koshelev, C. Cianciaruso, M. De Palma, Y. Kivshar, and H. Altug, Imaging-based spectrometer-less optofluidic biosensors based on dielectric metasurfaces for detecting extracellular vesicles, Nat. Commun. **12**, 3246 (2021).
[16] Y. Zhang, W. Liu, Z. Li, Z. Li, H. Cheng, S. Chen, and J. Tian, High-quality-factor multiple Fano resonances for refractive index sensing, Opt. Lett. **43**, 1842 (2018).

[17] R. Chai, W. Liu, Z. Li, H. Cheng, J. Tian, and S. Chen, Multiband quasibound states in the continuum engineered by space-group-invariant metasurfaces, Phys. Rev. B **104**, 075149 (2021).

[18] T. Santiago-Cruz, S. D. Gennaro, O. Mitrofanov, S. Addamane, J. Reno, I. Brener, and M. V. Chekhova, Resonant metasurfaces for generating complex quantum states, Science **377**, 991 (2022).

[19] J. Zhang, J. Ma, M. Parry, M. Cai, R. Camacho-Morales, L. Xu, D. N. Neshev, and A. A. Sukhorukov, Spatially entangled photon pairs from lithium niobate nonlocal metasurfaces, Sci. Adv. **8**, eabq4240 (2022).

[20] X. Gao, B. Zhen, M. Soljacic, H. Chen, and C. W. Hsu, Bound states in the continuum in fiber Bragg gratings, ACS Photonics **6**, 2996 (2019).

[21] K. Koshelev, A. Bogdanov, and Y. Kivshar, Meta-optics and bound states in the continuum, Sci. Bull. **64**, 836 (2019).

[22] S. Liu, H. Tong, and K. Fang, Optomechanical crystal with bound states in the continuum, Nat. Commun. **13**, 3187 (2022).

[23] R. Chai, Q. Liu, W. Liu, Z. Li, H. Cheng, J. Tian, and S. Chen, Emerging planar nanostructures involving both local and nonlocal modes, ACS Photonics **10**, 2031 (2023).

[24] K. Koshelev, S. Lepeshov, M. Liu, A. Bogdanov, and Y. Kivshar, Asymmetric metasurfaces with high-Q resonances governed by bound states in the continuum, Phys. Rev. Lett. **121**, 193903 (2018).

[25] J. Jin, X. Yin, L. Ni, M. Soljačić, B. Zhen, and C. Peng, Topologically enabled ultrahigh-Q guided resonances robust to out-of-plane scattering, Nature (London) **574**, 501 (2019).

[26] M. Kang, S. Zhang, M. Xiao, and H. Xu, Merging bound states in the continuum at off-high symmetry points, Phys. Rev. Lett. **126**, 117402 (2021).

[27] M. Kang, L. Mao, S. Zhang, M. Xiao, H. Xu, and C. T. Chan, Merging bound states in the continuum by harnessing higher-order topological charges, Light: Sci. Appl. **11**, 228 (2022).

[28] Z. Chen, X. Yin, J. Jin, Z. Zheng, Z. Zhang, F. Wang, L. He, B. Zhen, and C. Peng, Observation of miniaturized bound states in the continuum with ultra-high quality factors, Sci. Bull. **67**, 359 (2022).

[29] S.-G. Lee, S.-H. Kim, and W.-J. Lee, Merging and band transition of bound states in the continuum in leaky-mode photonic lattices, Laser Photonics Rev. **17**, 2300550 (2023).

[30] B. Zhen, C. W. Hsu, L. Lu, A. D. Stone, and M. Soljačić, Topological nature of optical bound states in the continuum, Phys. Rev. Lett. **113**, 257401 (2014).

[31] J. Lv, Z. Chen, X. Yin, Z. Zhang, W. Hu, and C. Peng, High-sensitive refractive index sensing enabled by topological charge evolution, IEEE Photonics J. **12**, 1 (2020).

[32] Z. Wang, J. Sun, J. Li, L. Wang, Z. Li, X. Zheng, and L. Wen, Customizing 2.5D out-of-plane architectures for robust plasmonic bound-states-in-the-continuum metasurfaces, Adv. Sci. **10**, 2206236 (2023).

[33] S. Li, B. Ma, Q. Li, and M. V. Rybin, Antenna-based approach to fine control of supercavity mode quality factor in metasurfaces, Nano Lett. **23**, 6399 (2023).

[34] A. C. Overvig, S. Shrestha, and N. Yu, Dimerized high contrast gratings, Nanophotonics **7**, 1157 (2018).

[35] W. Wang, Y. K. Srivastava, T. C. Tan, Z. Wang, and R. Singh, Brillouin zone folding driven bound states in the continuum, Nat. Commun. **14**, 2811 (2023).

[36] G. Xu, A. Overvig, Y. Kasahara, E. Martini, S. Maci, and A. Alù, Arbitrary aperture synthesis with nonlocal leaky-wave metasurface antennas, Nat. Commun. **14**, 4380 (2023).

[37] H. Huang, A. C. Overvig, Y. Xu, S. C. Malek, C.-C. Tsai, A. Alù, and N. Yu, Leaky-wave metasurfaces for integrated photonics, Nat. Nanotechnol. **18**, 580 (2023).

[38] D. R. Abujetas, N. Van Hoof, S. ter Huurne, J. G. Rivas, and J. A. Sánchez-Gil, Spectral and temporal evidence of robust photonic bound states in the continuum on terahertz metasurfaces, Optica **6**, 996 (2019).

[39] Y. Zeng, G. Hu, K. Liu, Z. Tang, and C.-W. Qiu, Dynamics of topological polarization singularity in momentum space, Phys. Rev. Lett. **127**, 176101 (2021).

[40] P. Hu, J. Wang, Q. Jiang, J. Wang, L. Shi, D. Han, Z.-Q. Zhang, C. T. Chan, and J. Zi, Global phase diagram of bound states in the continuum, Optica **9**, 1353 (2022).

[41] L. Ni, J. Jin, C. Peng, and Z. Li, Analytical and statistical investigation on structural fluctuations induced radiation in photonic crystal slabs, Opt. Express **25**, 5580 (2017).

[42] X. Yin, J. Jin, M. Soljačić, C. Peng, and B. Zhen, Observation of topologically enabled unidirectional guided resonances, Nature (London) **580**, 467 (2020).

[43] H. S. Nguyen, F. Dubois, T. Deschamps, S. Cueff, A. Pardon, J.-L. Leclercq, C. Seassal, X. Letartre, and P. Viktorovitch, Symmetry breaking in photonic crystals: On-demand dispersion from flatband to dirac cones, Phys. Rev. Lett. **120**, 066102 (2018).

[44] S. Xiao, M. Qin, J. Duan, F. Wu, and T. Liu, Polarization-controlled dynamically switchable high-harmonic generation from all-dielectric metasurfaces governed by dual bound states in the continuum, Phys. Rev. B **105**, 195440 (2022).

[45] M. Qin, J. Duan, S. Xiao, W. Liu, T. Yu, T. Wang, and Q. Liao, Strong coupling between excitons and quasibound states in the continuum in bulk transition metal dichalcogenides, Phys. Rev. B **107**, 045417 (2023).

[46] L. Huang, S. Li, C. Zhou, H. Zhong, S. You, L. Li, Y. Cheng, and A. E. Miroshnichenko, Realizing ultrahigh-Q resonances through harnessing symmetry-protected bound states in the continuum, Adv. Funct. Mater. (2023), doi:10.1002/adfm.202309982.